Ultrasonics Sonochemistry 108 (2024) 106952

Contents lists available at ScienceDirect

Ultrasonics Sonochemistry

journal homepage: www.elsevier.com/locate/ultson

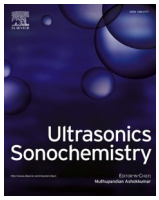

Investigation of mechanisms of shock wave generation by collapse of cavitation bubbles near particles

Jinsen Hu [a], Yifan Liu [a], Jingfei Duan [a], Jiaxin Yu [a,*], Yuning Zhang [a,*], Dan Gao [a], Yuning Zhang [b,c]

[a] Key Laboratory of Power Station Energy Transfer Conversion and System (Ministry of Education), School of Energy Power and Mechanical Engineering, North China Electric Power University, Beijing 102206, China
[b] College of Mechanical and Transportation Engineering, China University of Petroleum–Beijing, Beijing 102249, China
[c] Beijing Key Laboratory of Process Fluid Filtration and Separation, China University of Petroleum–Beijing, Beijing 102249, China

ARTICLE INFO

Keywords:
Cavitation bubble dynamics
Shock waves
Particle-bubble interaction
Jet dynamics

ABSTRACT

The mechanism of generation of shock waves by the collapse of a cavitation bubble near a single particle or dual particles is numerically investigated using OpenFOAM. For the single-particle case, shock waves during bubble inception and jet impacting on the particle surface are revealed in detail. The pressure induced on the particle by the inception shock wave of the bubble decreases with increasing bubble-particle distance, and the pressure is proportional to $1/r^{1.26}$ (r being the distance from the center of the shock wave). For the dual particles, the evolution of the neck structure is closely related to the generation mechanism of the shock wave. At extremely close particle–bubble distances, two shock waves propagating in opposite directions are emitted outside and inside the bubble after two necks collide. At long particle–bubble distances, a shock wave is emitted after the neck contracts, and simultaneously the bubble splits into two daughter bubbles. The energy of the shock wave generated by the neck constriction (i.e., the pressure at its generation location) first increases and then decreases with increasing bubble-particle distance. For unequal-sized double particles, the size of the daughter bubble depends on the bubble-particle distance and the particle size. These findings provide new perspectives for understanding the damage sustained by hydro-mechanical components operating in sand-laden water flows.

1. Introduction

For hydraulic machinery operating in sand-laden flows, sand particles and nearby cavitation bubbles show substantial effects on the service life and safety of the units [1–4]. Extensive research proofed that the jets and shock waves generated by cavitation bubbles adjacent to a rigid wall (as a simplified representation of the hydro-mechanical component) are the main cause of damage to the components [5–8]. However, the presence of particles may also alter the shock waves and jets released from cavitation bubbles [9,10]. Therefore, in the present paper, the behavior of shock waves generated by bubble collapse adjacent to a single particle and to dual particles are investigated by a numerical approach (with the aid of OpenFOAM) to elucidate the shock wave dynamics.

Shock waves associated with cavitation bubbles can be classified into two types: those generated by a single cavitation bubble and those generated by cavitation bubbles adjacent to boundaries (e.g., flat walls). In the case of shock waves emitted by a single cavitation bubble formed by laser acting on water, Vogel et al. [11] investigated the relationship between shock wave propagation behavior and laser properties. Their results revealed that a large laser energy and long laser duration increases the pressure, duration, energy, and width of the shock waves. Using a numerical approach combining the Kirkwood–Bethe hypothesis and the Gilmore model, Lai et al. [12] revealed that the velocity of a laser-induced shock wave is highly attenuated and the normalized shock wave width is not correlated with the duration or energy of the laser. Geng et al. [13] proposed a predictive model for wave front localization combining bubble growth and shock wave propagation, which was validated by the experimental data from Vogel and Busch [11]. The laser-induced bubble produces shock waves with extremely high velocities upon its formation and collapse. When a single cavitation bubble inception, Noack and Vogel [14] observed maximum shock wave velocities of 4700 m/s and 5400 m/s at laser energies of 1 mJ and 10 mJ, respectively. Liang et al. [15] further developed a hybrid experimental/simulation approach to evaluate the shock wave properties of a laser-

* Corresponding authors.
E-mail addresses: yujiaxin1012@foxmail.com (J. Yu), yuning.zhang@foxmail.com (Y. Zhang).

https://doi.org/10.1016/j.ultsonch.2024.106952
Received 20 February 2024; Received in revised form 9 June 2024; Accepted 11 June 2024
Available online 12 June 2024
1350-4177/© 2024 The Authors. Published by Elsevier B.V. This is an open access article under the CC BY-NC-ND license (http://creativecommons.org/licenses/by-nc-nd/4.0/).

Nomenclature

Abbreviations

BCSW	Bubble-collapse shock wave
BRSW	Bubble-reflected shock wave
ISW	Inception shock wave
JIPSW	Jet impact particle shock wave
JPSW	Jet-pierce shock wave
JTSW	Jet-tip shock wave
NCSW	Neck-contraction shock wave
PRSW	Particle-reflected shock wave
RJTSW	Reflected jet-tip shock wave
TNCSW	Two-neck collision shock wave
VOF	Volume of fluid

Subscripts

w	Water phase
b	Bubble phase
p_1	Particle 1
p_2	Particle 2

Symbols

C_v	Heat capacity (J/(kg·K))
C_w	Liquid constant for the water state (J/kg·K)
$\boldsymbol{F}_s$	Surface tension of water (N/m)
K	Kinematic energy (J)
L	Shortest distance from surface of two particles (mm)
l	Shortest distance between point of bubble inception and particle surface (mm)
$\dot{m}$	Rate of mass transfer between water and bubble (kg/s)
p	Pressure (Pa)
p_w	Pressure constant for the water state (Pa)
R_b	Vapor constant for bubble state J/(kg·K)
$R_{\max}$	Maximum radius of bubble (mm)
R_{p1}	Radius of single particle or of larger particle for unequal-sized dual particles (mm)
R_{p2}	Radius of small particle for unequal-sized dual particles (mm)
t	Time (s)
T	Temperature (K)
T_w	Temperature constant for the water state (K)
$\boldsymbol{U}$	Velocity (m/s)
$\boldsymbol{U}_r$	Relative velocity between the two phases (m/s)
W	Width of panel in figure (mm)

Greek

α	Volume fraction
γ	Dimensionless bubble–particle distance
δ	Ratio of the radii of larger and smaller particles
η	Ratio of R_{p1} to maximum radius of bubble
ρ	Density of fluid (kg/m^3)
τ	Viscous stress tensor (Pa)
ψ	Compressibility of fluid

induced bubble. In the experimental part, the plasma size is taken as input and the bubble oscillation period is taken as fitting parameter, and in the simulation part, the extended Gilmore model and van der Waals hard core law are combined. At a laser duration of 6 ns and a laser energy of 10 mJ, the velocity of the bubble shock wave estimated by this hybrid method is about 5000 m/s. When a cavitation bubble collapse, Holzfuss et al. [16] utilizing the Gilmore model and the Kirkwood-Bethe hypothesis found that the shock wave reached a velocity of 4000 m/s. Pecha and Gompf [17] further verified this result utilizing the streak camera and found that the shock wave intensity decays faster than $1/r$ (where r is the distance to the center of the shock wave). Compared with individual bubble dynamics models (e.g., Rayleigh-Plesset equation, Gilmore equation, and Keller-Miksis equation) [18,19], the unified theory of bubble dynamics proposed by Zhang et al. [20] takes into account the effects of different boundaries and enables the prediction of the shock wave characteristics of bubbles near the boundaries.

For investigating shock waves from cavitation bubbles adjacent to boundaries, a flat rigid wall provides a representative case [21,22]. Depending on the stand-off distance (the dimensionless bubble–wall distance), the generation mechanisms of the shock wave can be categorized into three scenarios. In the first scenario, the stand-off distance is extremely close, and the bubble generates a "kink" structure during its collapse [23]. When the fluid around the "kink" collides, shock waves are emitted from the point of collision. In the second scenario, the bubble comes into contact with the wall at its maximum volume and produces a jet directed toward the wall during its collapse [24]. Zhang et al. [25] found that the shock waves from the jet impinging on a wall are reflected by the wall, which in turn generates a tension wave. In addition, the low-pressure region generated by the tension wave tends to produce cavitation bubbles, which in turn leads to the formation of a counter-jet. Further, Tian et al. [26] found that two sub-annular bubbles (sub-bubbles with an annular shape formed after the jet penetrating the bubble) emit shock waves upon rebound and collapse. In the third scenario, the stand-off distance is large, and the jet does not impact the wall. On the basis of results from Yang et al. [27] the generation of shock waves in this case can be summarized as follows. First, the jet tip forms a shock wave in the bubble, which passes through the bubble and produces a precursor shock wave. Then, the jet produces a water-hammer shock wave when it penetrates the bubble. Finally, the water-hammer shock wave merges with the precursor shock wave and propagates toward the wall. Požar and Agrež [28] found that the concave wall causes refocusing of bubble-induced shock waves and triggers the secondary cavitation adjacent to the focus.

Regarding the shock waves resulting from the collapse of bubble pair, Fan et al. [29] concentrated on bubble pair of identical energy with antiphase in a narrow dimensionless distance range. The growth of the second bubble causes the first bubble to collapse in a toroidal shape, and generates the toroidal shock waves. This shock waves enhance the radial flow of the liquid around the neck of the second bubble. Subsequently, the liquid jet generated by the neck contraction to the axis of symmetry produces a conical shock wave with a half cone angle of 16° inside the bubble. Yang et al. [30] investigated the shock waves caused by the collapse of bubble pair with different phases and energies at large dimensionless distance values. The shock waves from the collapse of the first bubble exhibit different attenuation in the directions approaching and moving away from the other bubble. Further, they explored the effect of the collapse shock waves of bubble pair on the wall. When the bubble pair horizontally arranged, their shock waves exerted substantial pressure on the wall. Conversely, when the bubble pair vertically arranged, the shock waves produced by their collapse results in pressure peaks on the wall that were generally lower than those generated by the collapse of a single bubble [31]. Investigations have also been performed for the shock waves generated by bubbles adjacent to different kinds of boundaries, such as an air bubble [32], ice [33], a free surface [34], and an air bubble on a tube nozzle [35].

Compared to the rigid wall, particles provide a limited length boundary for bubbles, which exhibit different collapse and jet behaviors. For a bubble in the vicinity of a single rigid particle, at short bubble-particle distances, it collapses with a mushroom shape and produces a jet directed toward the particle [36]. At long bubble-particle distances, it

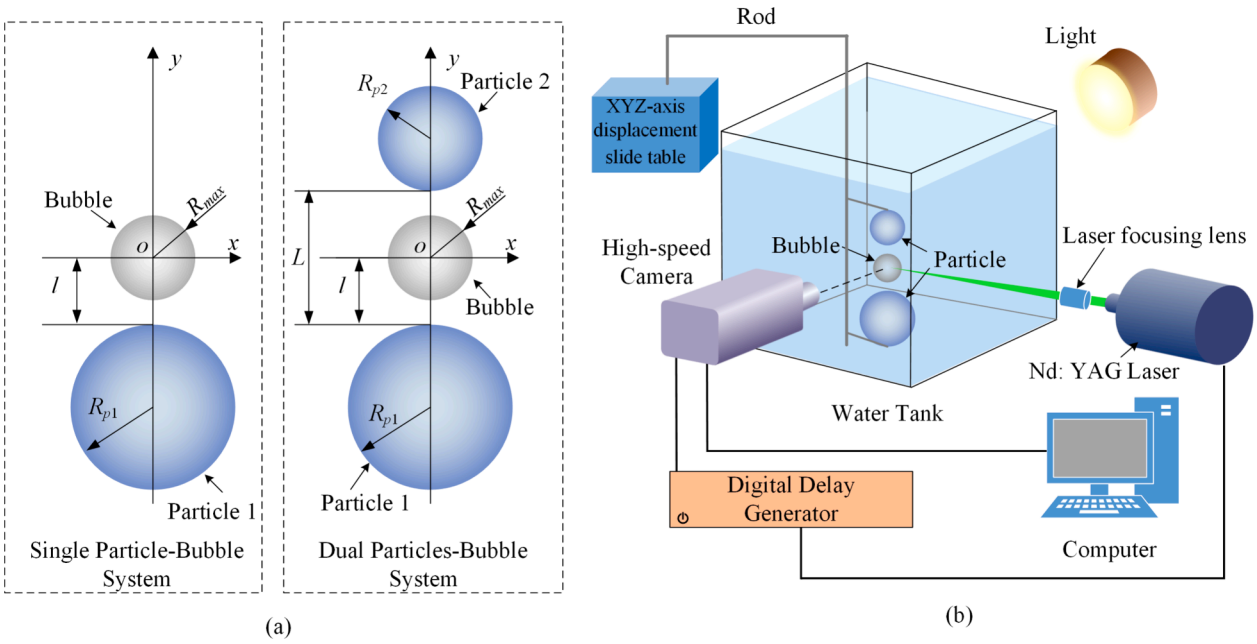

Fig. 1. (a) Schematics of particle and cavitation bubble arrangements. (b) Schematic of experimental platform.

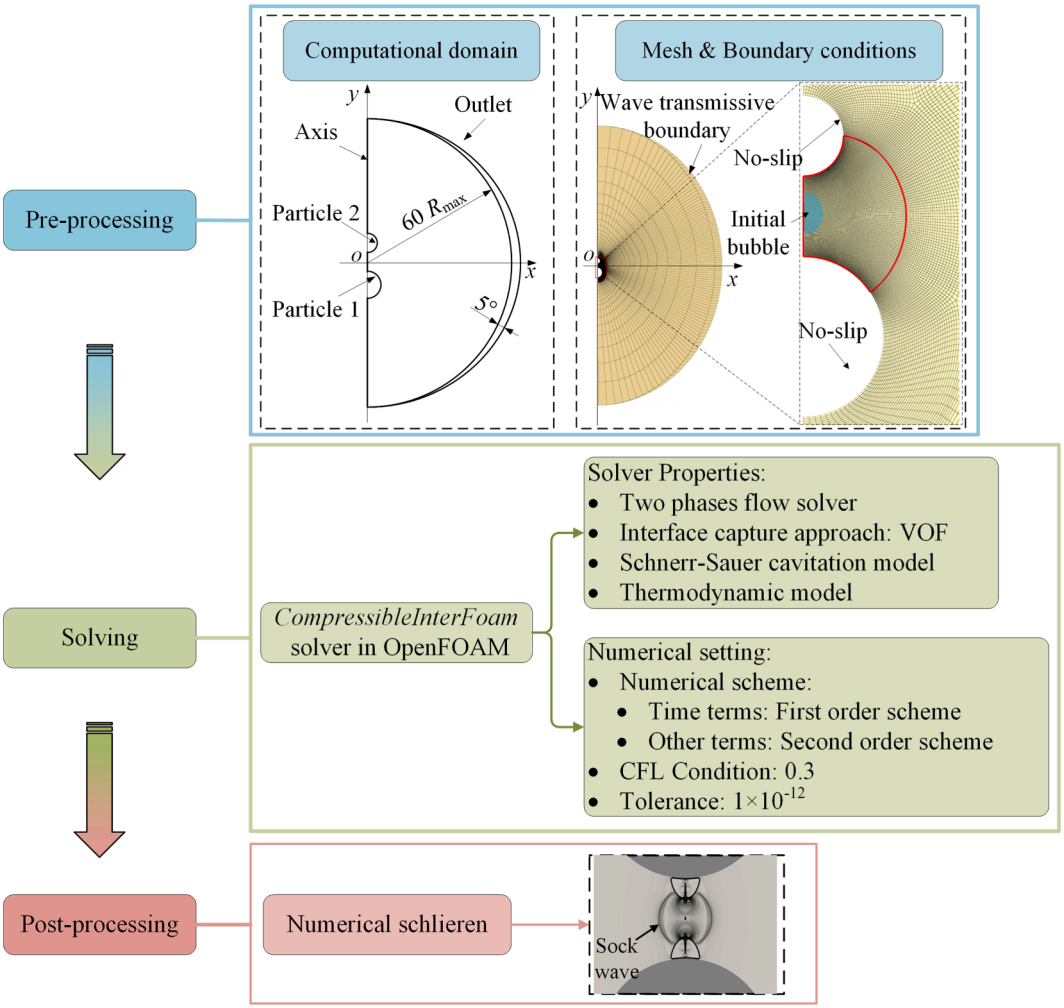

Fig. 2. Numerical simulation flow for bubble oscillation and shock waves.

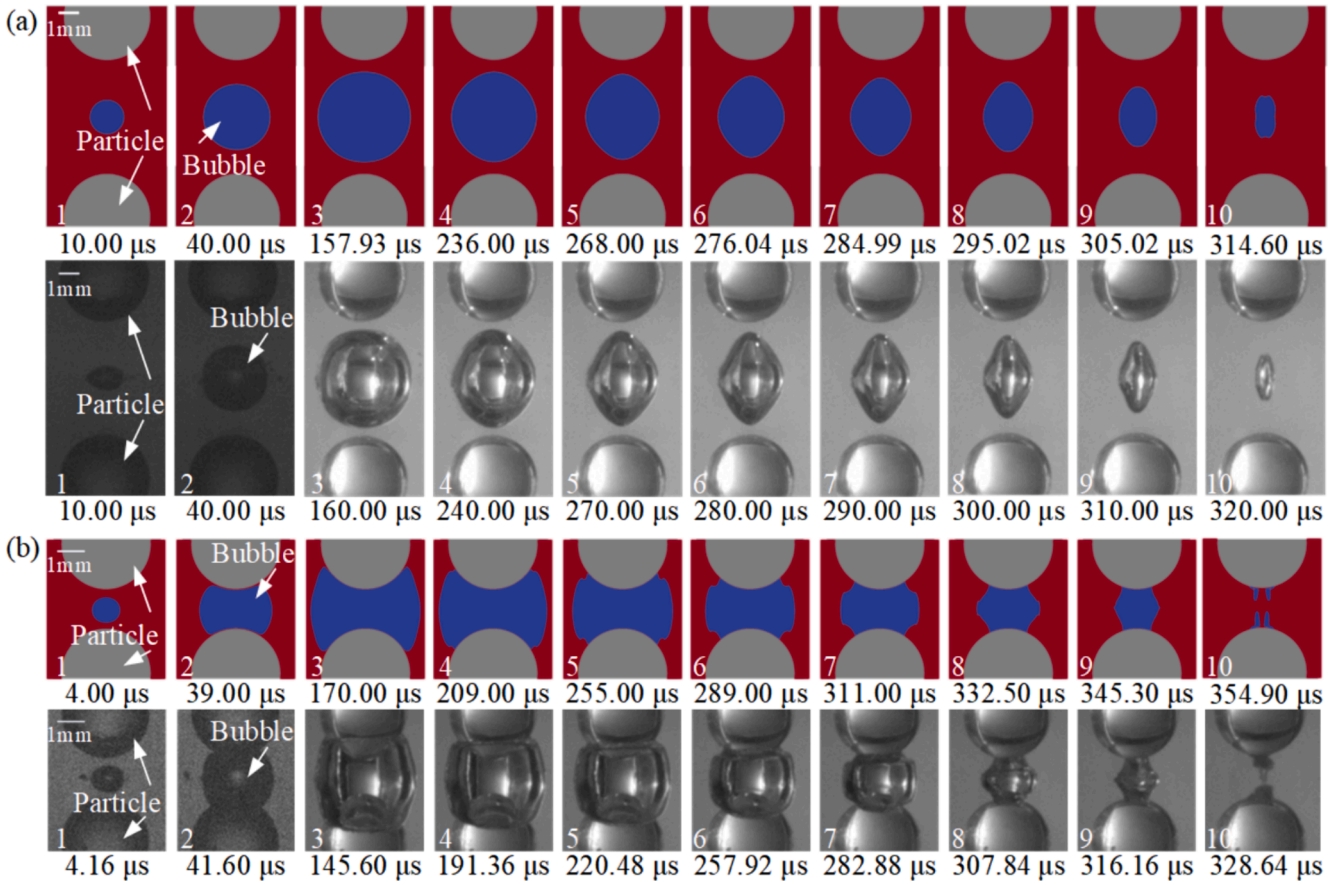

Fig. 3. Experimental validation of numerical method. (a) $\gamma = 1.23$, $\eta = 0.94$ mm. [52] (b) $\gamma = 0.42$. $\eta = 0.94$. The first row of each subplot shows the simulation results, and the second row shows the experimental results. In the simulated results, gray, red and blue areas represent particles, water and bubble, respectively. R_{max} = 1.60 mm.

produces dual jets approaching each other, where the jet close to the particle moves away from the particle [37]. When a bubble oscillates near an elastic particle, its expansion and collapse cause the elastic particle to be compressed and stretched, respectively. The magnitude of deformation in particle is dependent on its elastic modulus, with a lower elastic modulus leading to greater elastic deformation [38]. For a movable particle, Poulain et al. [39] explored the particle velocity law caused by bubble collapse. Their results revealed that the particle velocity is inversely related to its density and radius, and directly proportional to the negative fourth power of the distance between the bubble and the particle. Teran et al. [40] numerically investigated the particle impact velocity inside a bubble driven by a jet. Based on the numerical results, they proposed a predictive model for particle impact velocity related to particle mass and particle position. Chen et al. [41] investigated the collapse behavior of a spark-induced bubble between two particles. Their observations indicated that when the particles are equal in size, the bubble tends to collapse at its original location. However, in the case of particles with unequal sizes, the bubble collapses toward one of the particles.

The investigation of shock waves adjacent to particles will also be briefly reviewed here. Zevnik and Dular [42] numerically studied the propagation of bubble-collapse shock waves adjacent to a single spherical particle at long particle–bubble distances. After the bubble collapses, the bubble-collapse shock wave impacts the particle surface and is reflected to form a tension wave, which then passes through the rebounding bubble. Zou et al. [43] experimentally explored the effect of single-particle shape (expressed as the ratio ζ between the long and short axes of an elliptical particle) on shock waves. For close particle–bubble distances, they found that the spatial and the temporal delays between the implosion shock wave (caused by bubble rebound) and the water-hammer shock wave leads to the stratification of shock waves. For long particle–bubble distances, only an implosion shock wave is generated without shock wave stratification. With increasing ratio ζ (i.e., the particle with a slender ellipsoid shape), the influence of the particle on the attenuation of shock wave intensity exhibits a decreasing trend. On the basis of this literature review, we find that the generation mechanism of bubble shock waves near particles has not been fully revealed.

In the present paper, bubble shock waves adjacent to a single particle and to dual particles are investigated by numerical simulations. The remainder of the paper is organized as follows. Section 2 introduces the particle–bubble system and the experimental platform. Section 3 compares the numerical and the experimental results. Section 4 presents the basic setups of the numerical simulation, including the computational domain, mesh, solver, and visualization approach for shock waves. Section 5 describes the shock waves during bubble inception and bubble collapses adjacent to a single particle. Section 6 discusses the bubble shock waves between two particles of equal size. Section 7 discussed the bubble shock waves between two particles of unequal size and the resulting interference phenomenon. Section 8 presents the main conclusions of the present research.

2. Particle–bubble system and experimental platform

Fig. 1(a) shows the schematic of the particle and bubble arrangements. For the single-particle–bubble system, the shortest distance between the point of bubble inception and the particle surface is denoted by l. The particle radius is denoted by R_{p1}. For the dual-particles–bubble

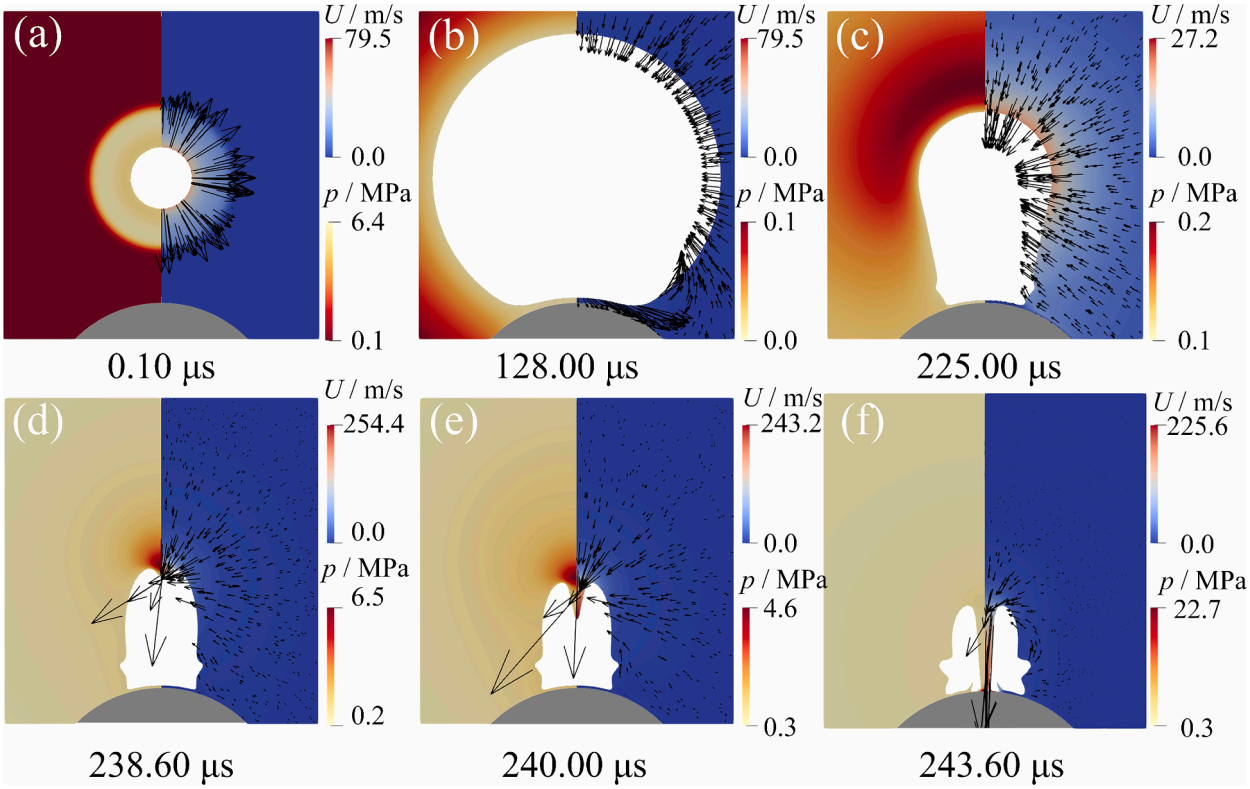

Fig. 4. Bubble interface evolution and jet development with liquid pressure distribution (left side of each frame) and liquid velocity distribution (right side of each frame) adjacent to a single particle. The black arrow in the velocity distribution indicates the velocity vector. The gray and the white areas represent the particle and the bubble, respectively. $\gamma = 0.90$. $\eta = 1.00$. $R_{max} = 1.15$ mm. $W = 2.60$ mm.

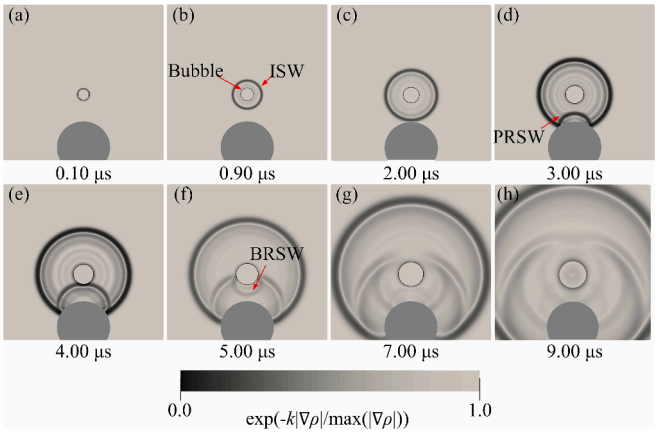

Fig. 5. Propagation of bubble inception shock wave during bubble inception adjacent to a single particle. The dark gray area is the particle. $\gamma = 0.90$. $\eta = 1.00$. $R_{max} = 1.15$ mm. $W = 2.00$ mm.

system, the bubble is generated at the midpoint between the two particles. The radius of the larger particle is denoted by R_{p1} and that of the smaller particle by R_{p2}, and the shortest distance from the surface of the two particles is denoted by L.

To assess the dynamics of the shock waves produced by bubbles near particles and to facilitate further analysis, four dimensionless parameters are defined as follows:

$$\gamma = \frac{l}{R_{max}} \tag{1}$$

$$\delta = \frac{R_{p1}}{R_{p2}} \tag{2}$$

$$\eta = \frac{R_{p1}}{R_{max}} \tag{3}$$

$$p^* = \frac{p}{p_\infty} \tag{4}$$

Here, γ represents the dimensionless bubble-particle distance. R_{max} indicates the maximum radius of the bubble. δ represents the ratio of the radii of the large particle to that of the small particle in the dual-particles–bubble system. η denotes the ratio of R_{p1} to R_{max}. p^* represents the dimensionless pressure normalized by the fluid pressure $p_\infty = 101325$ Pa at infinity.

Fig. 1(b) shows a schematic of the experimental platform for generating and recording cavitation bubbles adjacent to particles. The experimental procedure is briefly described below. The particles, made of SiO_2 with a density of 2500 kg/m^{3}and a radius of 1.5 mm, are connected to the XYZ-axis displacement slide table through connecting rods. After the particles are immersed in deionized water, the XYZ-axis displacement slide table adjusts the relative positions of the particles and the bubble. The digital delay generator (ZKG027; minimum adjustment step: 0.15 ns) controls the Nd:YAG laser (Penny-100-S; wavelength: 532 nm; pulse duration: 5.4 ns) to emit a laser beam (Maximum laser energy: 30 mJ; laser diameter: 3 mm). When the laser beam passes through the laser focusing lens (LMH-10X-532; focal length: 20 mm) consisting of a concave lens and a convex lens, it is first expanded by the concave lens to enlarge the beam's diameter and enhance its collimation, followed by focusing it in deionized water to generate a cavitation bubble. In parallel, the digital delay generator also controls the high-speed camera (Phantom v1212; sample rate: 100,000 fps; image resolution: 256 × 256 pix) to record images of bubble

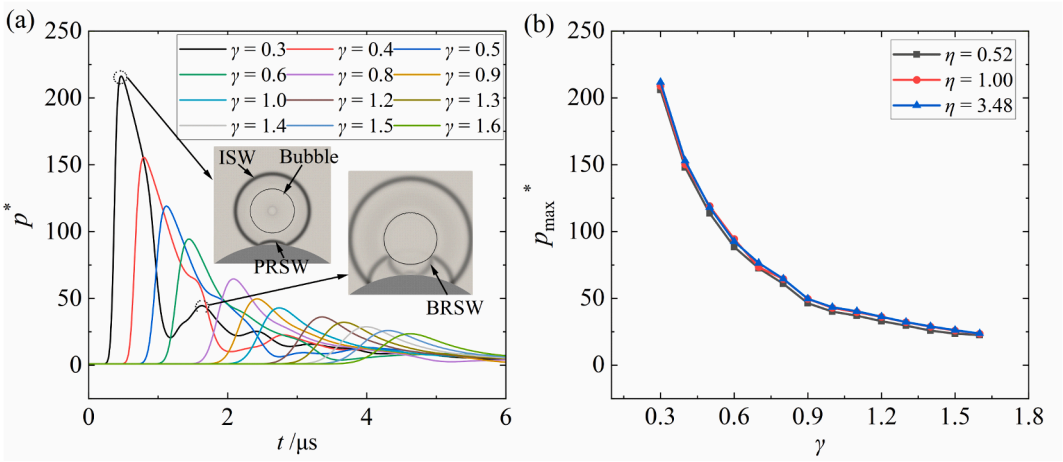

Fig. 6. Pressure variations at the upper apex of the particle induced by the inception shock wave (ISW) of the bubble. (a) Pressure variations with time for different bubble-particle distances. $\eta = 1.00$. (b) Effect of relative size (η) and relative distance (γ) between the bubble and the particle on the maximum pressure at the apex of the particle. $R_{max} = 1.15$ mm.

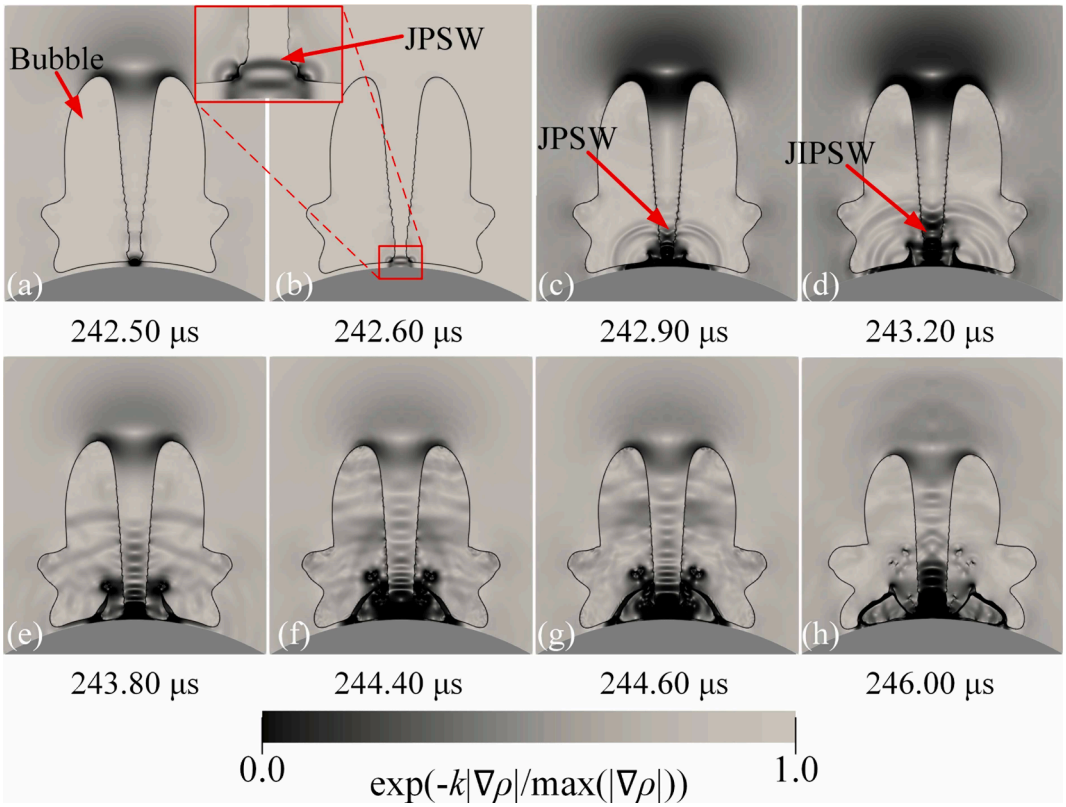

Fig. 7. Shock waves generated during the impact of the jet on the particle. The dark gray area is the particle. $\gamma = 0.90$. $\eta = 1.00$. $R_{max} = 1.15$ mm. $W = 1.00$ mm.

oscillation. These images are transferred to a computer for storage. The light enables the bubble image to be clearer and brighter. The laser beam is focused through a lens to a point 2 cm from the wall of the water tank, where it generates a bubble. Under ambient room temperature and particle-free conditions, the experimental system produced a bubble with a maximum radius (R_{max}) ranging from 1.0 mm to 1.8 mm.

3. Numerical methods for bubble and shock wave

Fig. 2 presents the numerical simulation setups of the bubble oscillation and shock waves. In the pre-processing stage, an axisymmetric computational domain is employed. The computational domain is a hemispherical region with a wedge angle of 5°, a maximum boundary of $60R_{max}$, and the Y-axis as the axis of symmetry. For the purpose of the accurate prediction, the mesh around the bubble and the particles is locally refined to accurately calculate the bubble interface. The refinement region is enclosed by the four red curves shown in the top subplot of Fig. 2. Adjusting the number of nodes on each of the four curves results in meshes with different levels of refinement. The first mesh height on the particle surface is 0.5 μm, and its mesh expansion in the normal direction is 1.2. On the basis of our previous work [44], a maximum mesh size of 2.4 μm is an appropriate choice in terms of computational accuracy and efficiency. When $\eta = 2.00$ and $\delta = 2.00$, the number of mesh cells is approximately 1.6 million for $\gamma = 0.25$ and approximately

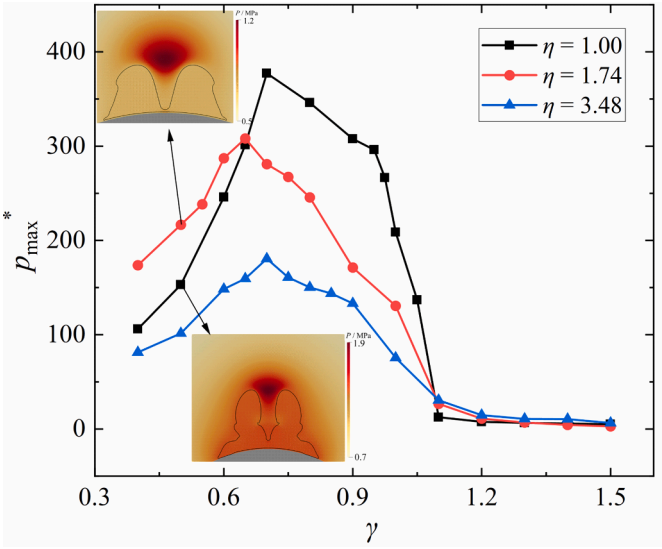

Fig. 8. Maximum pressure at the upper apex of the particle induced by the jet-pierce bubble shock wave (JPSW) as function of the relative sizes (η) and the relative distances (γ) between the particle and the bubble. $R_{max} = 1.15$ mm.

2.4 million for $\gamma = 0.35$. The initial bubble is resolved with about 83 mesh cells in the radial direction.

The boundary conditions for the particle surfaces and the outlet are no-slip and a wave transmissive boundary, respectively. A semicircular region with a radius of 0.2 mm is created as an initial bubble between the two particles. For the single particle, the computational domain and the boundary conditions are analogous to those of the dual particles–bubble system [45]. To simulate bubble growth, the pressure inside the initial bubble is set much higher than the surrounding pressure. In addition, by adjusting the pressure of the initial bubble, it is possible to obtain different values of R_{max}.

In the solution stage for bubble behavior, the *compressibleInterFoam* solver in OpenFOAM-v10 [46,47] is employed. This solver is a two-phase flow model that incorporates thermodynamic effects, fluid compressibility, and mass transfer. The solver employs a homogeneous mode to solve the system of control equations, and tracks the variation of the bubble interface via the fluid-volume method. Therefore, the continuity equation for the fluid is [26]

$$\frac{\partial \rho}{\partial t} + \nabla \bullet (\rho \boldsymbol{U}) = 0 \tag{5}$$

The continuity equation with mass transfer for water phase and bubble phase are [26]

$$\frac{\partial \alpha_w \rho_w}{\partial t} + \nabla \bullet (\alpha_w \rho_w \boldsymbol{U}) = \dot{m} \tag{6}$$

$$\frac{\partial \alpha_b \rho_b}{\partial t} + \nabla \bullet (\alpha_b \rho_b \boldsymbol{U}) = -\dot{m} \tag{7}$$

with

$$\alpha_w + \alpha_b = 1 \tag{8}$$

$$\rho = \alpha_w \rho_w + \alpha_b \rho_b \tag{9}$$

where α_w and α_b are the volume fractions of water phase and bubble phase in VOF method, respectively. ρ_w and ρ_b are the densities of water and bubble, respectively. ρ and $\boldsymbol{U}$ are the mixture density and the velocity of the mixture, respectively. t is the time. The rate of mass transfer $\dot{m}$ between the water and the bubble is obtained by the Schnerr–Sauer model [48,49].

The phase continuity equation is [26]

$$\frac{\partial \alpha_w}{\partial t} + \nabla \bullet (\alpha_w \boldsymbol{U}) + \nabla \bullet (\alpha_w \alpha_b \boldsymbol{U}_r) = \alpha_w \alpha_b \left(\frac{\psi_w}{\rho_w} - \frac{\psi_b}{\rho_b} \right) \frac{Dp}{Dt} + \dot{m} \left(\frac{1}{\rho_w} - \alpha_w \left(\frac{1}{\rho_w} - \frac{1}{\rho_b} \right) \right) + \alpha_w \nabla \bullet \boldsymbol{U} \tag{10}$$

with

$$\psi_w = \frac{d\rho_w}{dp} \tag{11}$$

$$\psi_b = \frac{d\rho_b}{dp} \tag{12}$$

where p is the pressure. ψ_w and ψ_b are the compressibility of water and bubble, respectively. $\boldsymbol{U}_r$ is the relative velocity between the water phase and the bubble phase.

The momentum and the energy equations are [26]

$$\frac{\partial \rho \boldsymbol{U}}{\partial t} + \nabla \bullet (\rho \boldsymbol{U}\boldsymbol{U}) = -\nabla p + \nabla \bullet \tau + \boldsymbol{F}_s \tag{13}$$

$$\frac{\partial \rho T}{\partial t} + \nabla \bullet (\rho \boldsymbol{U} T) = \nabla \bullet (K \nabla T) + \left[\nabla (p \boldsymbol{U}) + \frac{\partial \rho K}{\partial t} + \nabla (\rho \boldsymbol{U} K) \right] \left(\frac{\alpha_w}{C_{v,w}} + \frac{\alpha_b}{C_{v,b}} \right) \tag{14}$$

where $\boldsymbol{\tau}$ is the viscous stress tensor. $\boldsymbol{F}_s$ is the surface tension of water. T and K are the temperature and the kinematic energy of water and bubble. $C_{v,w}$ and $C_{v,b}$ are the heat capacities of water and bubble.

The equations of state for water proposed by Tammann [50] and ideal gas for bubble are shown below.

$$\rho_w = \frac{p + p_w}{C_w (T + T_w)} \tag{15}$$

$$\rho_b = \frac{p}{R_b T} \tag{16}$$

where the constants p_w, T_w, and C_w are the pressure, temperature, and liquid constants for the water state. R_b is the vapor constant for bubble state.

The numerical settings, such as water and bubble property parameters, numerical schemes, tolerances, and Courant numbers, are the same as in our previous work [45]. In the post-processing stage, the numerical schlieren [51] is adopted to demonstrate the shock waves. The expression for the schlieren value is $\exp(-k|\nabla\rho|/\max(|\nabla\rho|))$. The adjustable parameter k makes the shock wave clearer, and in this paper, it varies within the range $0 < k \leq 50$.

4. Experimental validation

Fig. 3 compares the simulated and the experimental evolutions of the bubble morphology adjacent to equal-sized dual particles. Two distinct distances between the bubble and the particle are chosen for examination. In Fig. 3(a), the bubble-particle distance is large, and the bubble expands in a spherical shape during its growth stage (frames 1–3). During the collapse stage (frames 4–10), the particles limit the contraction of the upper and the lower ends of the bubble, transforming the bubble from a spherical shape to an "olive shape". In Fig. 3(b), the bubble-particle distance is small, the upper and the lower ends of the bubble expand along the particle surface during the its growth stage (frames 1–3). During the collapse stage (frames 4–10), the bubble fractures from its center into two bubbles. Comparing the shape and the size of the bubble, the simulation results show close agreement with those of the experiment.

5. Shock waves adjacent to a single particle

Fig. 4 shows the bubble interface evolution and the jet development

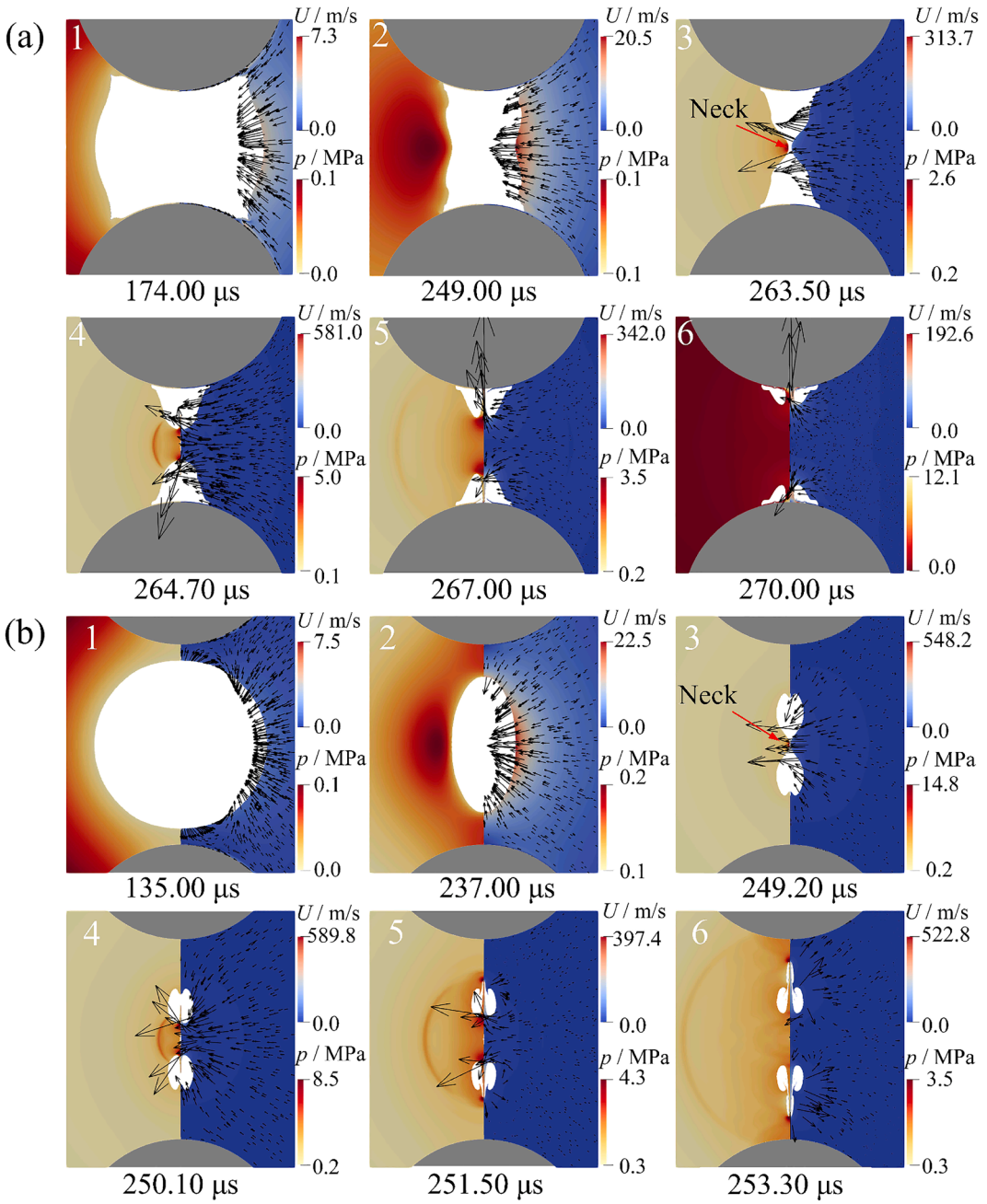

Fig. 9. Bubble interface evolution and jet development with liquid pressure distribution (left side of each frame) and liquid velocity distribution (right side of each frame) adjacent to dual particles of equal size. (a) $\gamma = 0.68$; (b) $\gamma = 1.19$. The black arrow indicates the velocity. The gray and the white areas represent the particle and the bubble, respectively. $\eta = 1.27$. $R_{max} = 1.18$ mm. $W = 2.60$ mm.

for a bubble adjacent to a single particle. When the bubble expands to its maximum size [Fig. 4(b)], the particle creates a crater at the bottom of the bubble. As shown in Fig. 4(c) and 4(e), with the collapse of the bubble, the liquid pressure above the bubble gradually increases. Consequently, the top of the bubble contracts with an accelerated velocity, evolving into a jet. Eventually, in Fig. 4(f), the jet impacts the particle surface.

Fig. 5 illustrates the propagation of the inception shock wave (ISW) during bubble inception adjacent to a single particle. The width of subgraph (W) is 2.00 mm. It can be seen from Fig. 5(a)–(c) that after bubble inception, the ISW propagates outward from the bubble inception position. In Fig. 5(d), when the ISW propagates to the particle surface, it is reflected to form a particle-reflected shock wave (PRSW). From Fig. 5(e)–(f), after the PRSW reaching the bubble interface, a bubble-reflected shock wave (BRSW) is formed. As shown in Fig. 5(g)–(h), the BRSW is reflected several times at both the bubble interface and the particle surface. The PRSW continues to propagate after passing through the bubble. The velocity of the shock wave is much greater than the speed of bubble growth.

Fig. 6 illustrates the pressure variations at the upper apex of the particle induced by the inception shock wave (ISW) of the bubble. Fig. 6 (a) demonstrates the pressure variations with time for different bubble-particle distances. When ISW impacts the particle, the pressure at the apex increases sharply and then decreases. The duration for the pressure increase is briefer than that for its decrease. As the shock wave propagates through the liquid, its energy progressively attenuate. Consequently, the maximum pressure induced by the ISW on the particle reduces with an increment in the bubble-particle distance. As PRSW

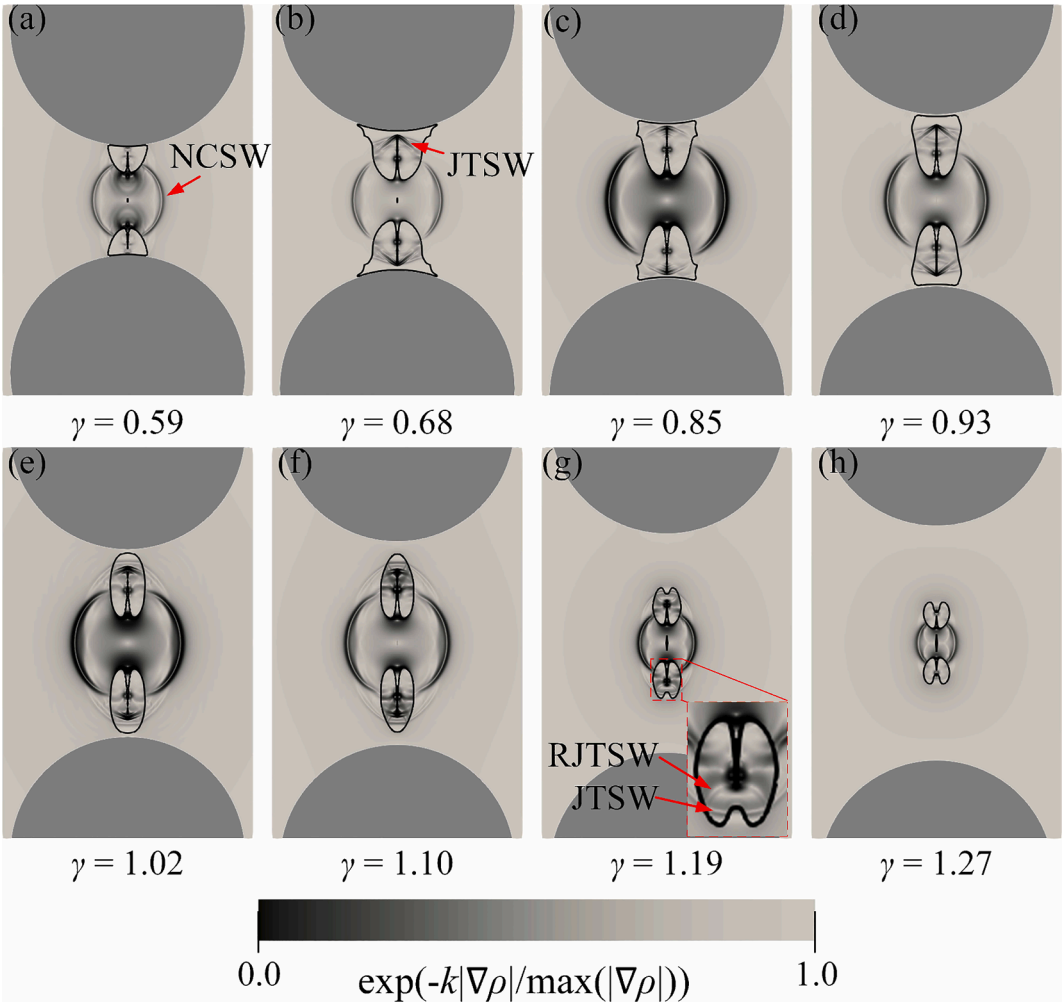

Fig. 10. Shock waves after the neck contraction for different values of γ: (a) $\gamma = 0.59$, $t = 264.10$ μs; (b) $\gamma = 0.68$, $t = 265.10$ μs; (c) $\gamma = 0.85$, $t = 249.90$ μs; (d) $\gamma = 0.93$, $t = 250.20$ μs; (e) $\gamma = 1.02$, $t = 248.30$ μs; (f) $\gamma = 1.10$, $t = 256.8$ μs; (g) $\gamma = 1.19$, $t = 250.20$ μs; (h) $\gamma = 1.27$, $t = 248.30$ μs. Dark gray areas are particles. $\eta = 1.27$. $R_{max} = 1.18$ mm. $W = 3.20$ mm.

propagates and is reflected between the particle and the bubble, its energy gradually decreases. Therefore, when PRSW impacts the particle, e.g., $\gamma = 0.3$ in Fig. 6(a), it induces a much lower pressure than ISW. As the bubble-particle distance increases, the pressure induced by BRSW decreases.

Fig. 6(b) demonstrates the influence of the relative sizes (η) and the relative distances (γ) between the bubble and the particle on the maximum pressure at the upper apex of the particle induced by ISW. In the figure, $R_{max} = 1.15$ mm, and an increase in η corresponds to an increase in the radius of the particle. As γ increases, the energy of ISW is gradually attenuated as the bubble-particle distance increases. Consequently, the pressure exerted by the ISW on the particle diminishes, which is proportional to $1/r^{1.26}$ (r being the distance from the center of the shock wave). Given that the intensity of the ISW is directly correlated with the bubble size, the influence of the particle size on the peak pressure induced by the ISW is relatively minor for the same bubble size.

Fig. 7 depicts the shock waves generated during the impact of the jet on the particle. According to the production mechanism of shock waves, two distinct categories of shock waves are formed. The first category is the jet-pierce bubble shock wave (JPSW), and the second is the jet impact particle shock wave (JIPSW). As demonstrated in Fig. 7(a)–(b), the JPSW is produced as the jet pierces the bubble. JPSW propagates both inside and outside the bubble, and its propagation direction is opposite to that of the jet. In Fig. 7(c)–(h), as the jet continuously impacts the top of the particle, the JIPSW is incessantly generated at the point of impact, and its propagation direction is also opposite to the jet. Temporally, the JPSW is generated prior to the JIPSW. Spatially, the JPSW is positioned ahead of the JIPSW. Combining Fig. 7(d)–(e) and Fig. 4(f), the shock wave inside the bubble first acts on the lower portion of the bubble causing it to expand, with its upper portion remaining contracted.

Fig. 8 illustrates the maximum pressure at the upper apex of the particle induced by the jet-pierce bubble shock wave (JPSW) as function of the relative distances (γ) and the relative sizes (η) between the bubble and the particle. The three maximum pressure curves exhibit a similar trend with γ. For $\gamma > 1.00$, the long bubble-particle distance causes the JPSW to travel a long path before impacting the particle. As a result, the JPSW generates a pressure that decreases as γ increases. For $\gamma \leq 1.00$, the maximum pressure shows an optimum around $\gamma = 0.75$. The jet velocity as it pierces the bubble initially increases with γ, reaches a maximum at $\gamma = 0.80$, and then decreases [45]. Consequently, the conversion of the kinetic energy of the jet into the JPSW's energy rises when $0.40 < \gamma \leq 0.75$ and falls when $0.75 < \gamma \leq 1.00$. The pressure generated by JPSW decreases with increasing η for the same γ, except for the cases $\eta = 1.00$, $0.4 < \gamma < 0.65$. Comparing the pressure distributions for $\eta = 1.00$ and $\eta = 1.74$ at $\gamma = 0.5$, it is observed that the internal pressure of the bubble is higher than the surrounding liquid at $\eta = 1.00$, the JPSW consequently induces less pressure compared to $\eta = 1.74$.

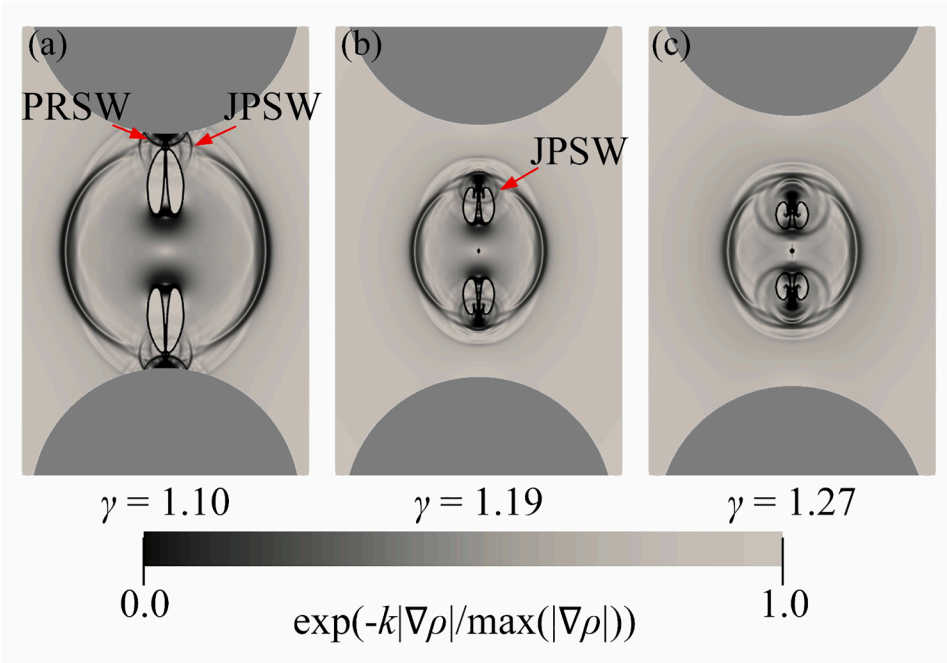

Fig. 11. Shock waves after the jet penetrating the bubble for different values of γ: (a) $\gamma = 1.10$, $t = 258.10$ μs; (b) $\gamma = 1.19$, $t = 251.20$ μs; (c) $\gamma = 1.29$, $t = 249.60$ μs. Dark gray areas are particles. $\eta = 1.27$. $R_{max} = 1.18$ mm. $W = 3.20$ mm.

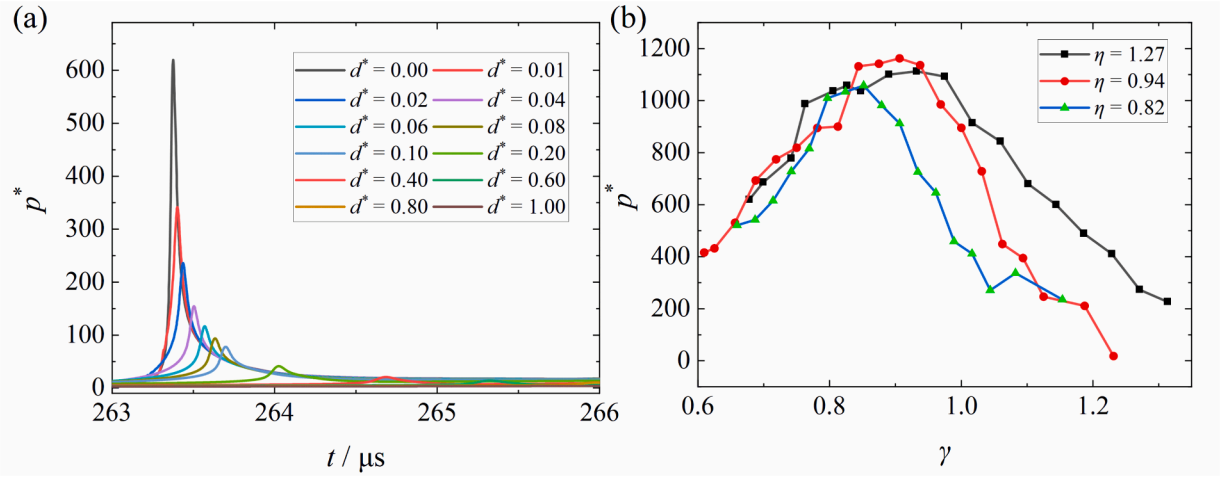

Fig. 12. Pressure variations on the X-axis induced by the neck contraction shock wave (NCSW). (a) Temporal evolution of the pressure induced by NCSW at different locations along the X-axis. $\gamma = 0.68$, $\eta = 1.27$, $R_{max} = 1.18$ mm. (b) Effect of the relative sizes and the relative distances between the bubble and the particles on pressure at $d^* = 0.00$ during NCSW generation.

6. Shock waves adjacent to equal-sized dual particles

Fig. 9 shows the bubble interface evolution and the jet development for a bubble adjacent to equal-sized dual particles during the collapse of the bubble. Based on the particle–bubble distance, two representative cases, namely, $\gamma = 0.68$ (particle–bubble distance less than R_{max}) and $\gamma = 1.18$ (particle–bubble distance greater than R_{max}) have been chosen to show the details of the bubble interface variations.

In Fig. 9(a), owing to the close particle–bubble distance, the bubble shows a highly non-spherical shape at its maximum. With the bubble contraction (frame 1–3), the liquid pressure around the middle of the bubble increases, and decreases from the middle of the bubble to the top or the bottom of the bubble. The non-uniform distribution of liquid pressure around the bubble results in the middle of the bubble interface contracting rapidly and evolving a neck structure. After that, the neck further contracts along the symmetry axis, and the bubble splits into two daughter bubbles (frame 4). As the two daughter bubbles experience the immense pressure generated by bubble splitting, a jet is consequently generated from each. After the jets inside the two daughter bubbles impinge on the particles (frame 5), they collapse in the vicinity of each of the two particles.

In Fig. 9(b), due to the long particle–bubble distance, the bubble shows an approximately spherical shape at its maximum (frame 1). From frame 2 to frame 3, the variations in liquid pressure around the middle of the bubble lead to the formation of the neck. At the same time, the increased pressure of the liquid above or below the bubble causes a depression shown at the top and the bottom of the bubble. From frame 4 to frame 6, the jets produced by the neck contraction move toward the depressions, piercing the bubble interface. Eventually, the daughter bubbles form two annular bubbles.

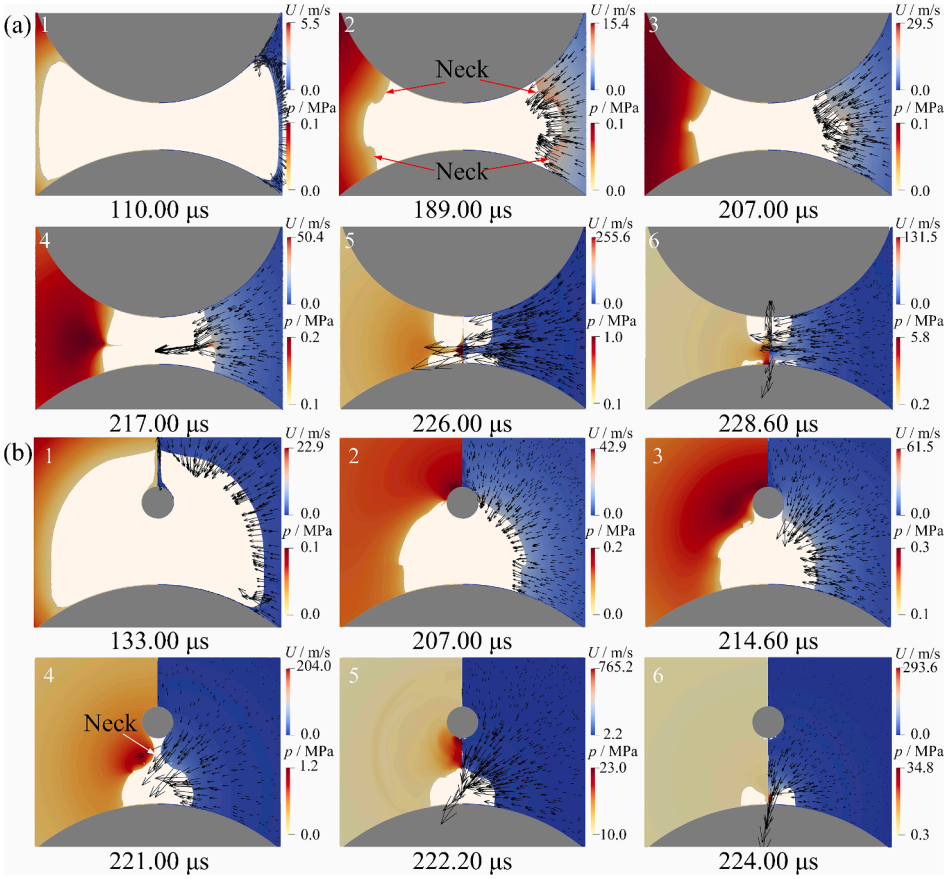

Fig. 13. Bubble interface evolution and jet development with liquid pressure distribution (left side of each frame) and liquid velocity distribution (right side of each frame) adjacent to equal-sized dual particles. (a) $\gamma = 0.25$, $\delta = 1.50$; (b) $\gamma = 0.35$, $\delta = 12.00$. The black arrow indicates the velocity. The gray and the white areas represent the particle and the bubble, respectively. $\eta = 2.00$. $R_{max} = 1.00$ mm. $W = 2.60$ mm.

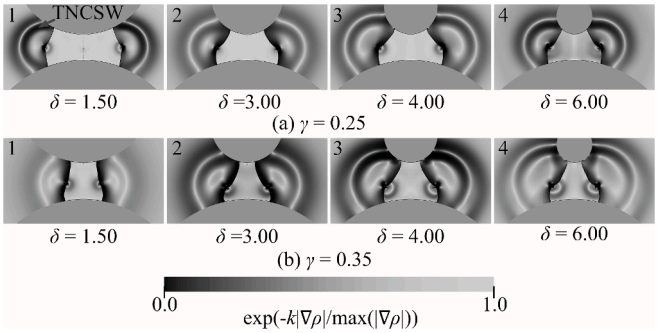

Fig. 14. TNCSW of bubble adjacent to unequal-sized dual particles for different values of γ and δ. (a) from left to right, $t = 210.80$ μs, 197.00 μs, 200.80 μs, 206.80 μs. (b) from left to right, $t = 206.00$ μs, 197.60 μs, 207.00 μs, 208.80 μs. Dark gray areas are particles. $\eta = 2.00$. $R_{max} = 1.00$ mm. $W = 3.00$ mm.

Fig. 10 illustrates the shock waves after the neck contraction. Eight cases have been chosen to demonstrate the effect of γ on the shock waves [with γ increasing from Fig. 10(a) to (h)]. From Fig. 10(a) to (g), two categories of shock waves were captured. The first category is the neck-contraction shock wave (NCSW), which is emitted from the position at which the neck contraction ends. The second category is the jet-tip shock wave (JTSW), which is emitted from the jet tip. It can be observed that the NCSW propagates in the liquid, and the JTSW propagates within the daughter bubble. In Fig. 10(g), the JTSW rapidly reaches the depression and is reflected to form a reflected JTSW (RJTSW). In Fig. 10(h), the jet reaches the depression quickly and does not capture the JTSW. As the NCSW scans across the interface of the two daughter bubbles, the high pressure at the wavefront surface will accelerate the contraction of the bubbles.

Fig. 11 illustrates the shock waves after the jet piercing the bubble interface for different values of γ. Three cases ($\gamma > 1.00$) have been chosen to show the shock waves. In Fig. 11(a), owing to the tiny spacing between the particle and the daughter bubble, the two jet-pierce bubble shock waves (JPSWs) quickly reach the particle surface, being reflected to form the PRSW afterwards. In Fig. 11(b), it is observed that the JPSWs are propagating in the water and inside the daughter bubbles. As shown in Fig. 11(c), two JPSWs pass through the daughter bubble and will interfere later. Moreover, Fig. 11(a)–(c) reveal the interference of the NCSW and two JPSWs.

Fig. 12 illustrates the pressure variations on the X-axis induced by the neck contraction shock wave (NCSW). The dimensionless distance d^* defined as the ratio of the distance d between a point on the X-axis and the location of shock wave generation to R_{max}. $d^* = 0.00$ indicates the location of NCSW. Fig. 12(a) illustrates the temporal evolution of the pressure induced by NCSW at different locations along the X-axis. When NCSW is generated, it causes a sharp rise in the liquid pressure. The pressure generated by the shock wave diminishes progressively over time and distance. When the shock wave reaches $d^* = 0.01$ from the generation position, its pressure attenuates from $619.59p_\infty$ to $341.70p_\infty$. As d^* increases, the attenuation of the shock wave pressure decreases.

Fig. 12(b) illustrates the effect of the relative sizes and the relative distances between the bubble and the particles on pressure at $d^* = 0.00$ when generating NCSW. In the figure, the radii $R_p = 1.50$ mm for both particles, and a decrease in η indicates an increase in R_{max}. As γ increases, the pressure at NCSW generation initially rises and

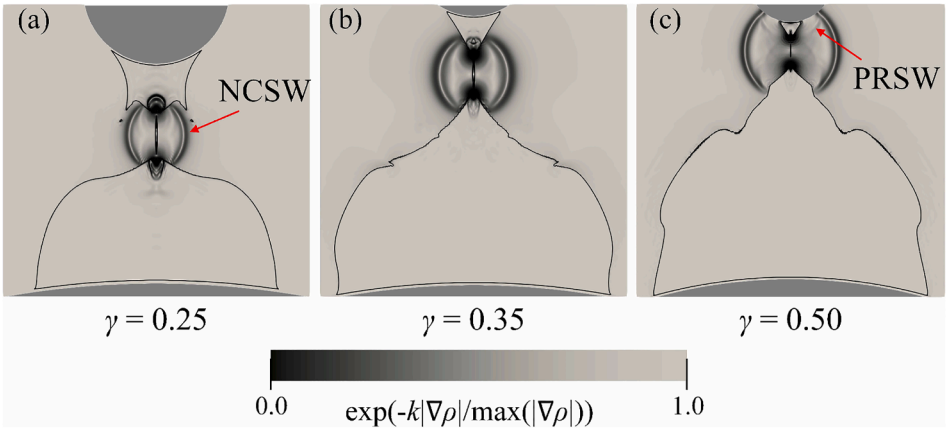

Fig. 15. The neck-contraction shock wave (NCSW) of bubble adjacent to unequal-sized dual particles for different values of γ: (a) $t = 224.30$ μs, $W = 0.70$ mm; (b) $t = 221.60$ μs, $W = 0.80$ mm; (c) $t = 214.15$ μs, $W = 1.20$ mm. Dark gray areas are particles. $\delta = 12.00$. $\eta = 2.00$. $R_{max} = 1.00$ mm.

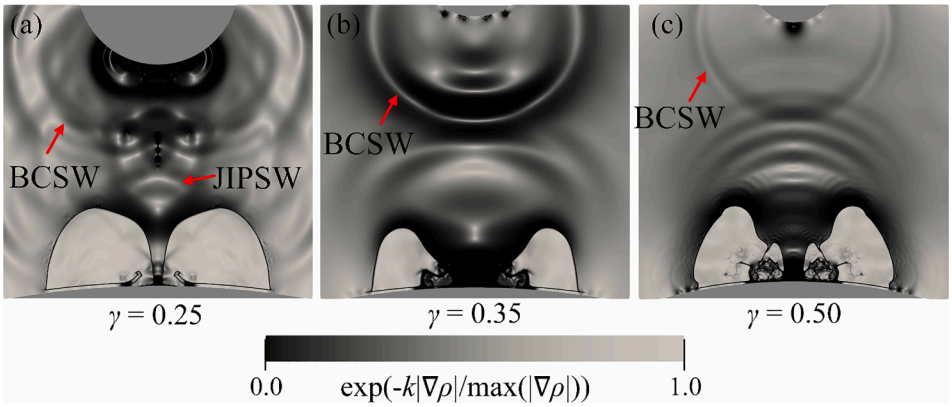

Fig. 16. Interference of bubble-collapse shock wave (BCSW) with jet-impact particle shock wave (JIPSW) adjacent to unequal-sized dual particles for different values of γ and δ. (a) $\delta = 11.00$, $t = 224.00$ μs, $W = 0.70$ mm; (b) $\delta = 12.00$, $t = 224.60$ μs, $W = 0.80$ mm; (c) $\delta = 12.00$, $t = 221.20$ μs, $W = 1.2$ mm. Dark gray areas are particles. $\eta = 2.00$. $R_{max} = 1.00$ mm.

subsequently declines, with a peak occurring near $\gamma = 0.9$. When $\gamma > 0.9$, the effect of the particles on the bubble contraction decreases as γ increases, causing the bubble contraction spherically. This phenomenon implies that the pressure inside the bubble tends to increase uniformly, which slows down the neck contraction, consequently reducing the energy (i.e., pressure) of NCSW as γ increases. For $\gamma < 0.9$, the particles significantly impact bubble contraction, causing the upper and the lower portions of the bubble to contract slower than its middle portion. As γ increases, the distance from the upper and the lower portions of the bubble to its center increases, which provides more space for the high pressure at the center of the bubble (caused by the neck contraction) to develop towards the upper and the lower portions of the bubble. Consequently, for this parameter zone, the pressure of NCSW increases with γ. As η decreases, the impact of particles on the bubble diminishes, consequently reducing the pressure of NCSW.

7. Shock waves adjacent to unequal-sized dual particles

Fig. 13 shows the bubble interface evolution and the jet development for a bubble adjacent to unequal-sized dual particles during the collapse of the bubble. Two representative cases have been chosen to show the effect of γ and δ on the variations of the bubble interfaces. In Fig. 13(a), owing to the extremely close particle–bubble distance, the bubble evolves two necks (frame 2). The high-pressure liquid surrounding the necks causes them to collide. Following the collision, an annular depression forms at the middle of the bubble (frame 4). Inside the annular depression, the liquid velocity is significantly higher than other positions. When the depression collides along the symmetry axis, the bubble evolves into two daughter bubbles of different sizes. Eventually, the jet generated inside the daughter bubble impacts the particle.

In Fig. 13(b), there is a considerable difference in size between the dual particles. When the bubble is at its maximum (frame 1), it almost wraps around the small particle. From frame 2 to frame 4, the high-pressure liquid above the small particle causes the bubble interface to rapidly contract and form a neck structure. Subsequently, in frame 5, the neck contracts along the symmetry axis, dividing the bubble into two daughter bubbles of notably different sizes. The tiny bubbles quickly collapse and rebound. For the enormous daughter bubble, the jet inside it impinges on the large particle.

Fig. 14 illustrates the two-neck collision shock wave (TNCSW) of a bubble adjacent to unequal-sized dual particles. Two groups of γ each with four values of δ have been chosen to demonstrate the TNCSW in detail. In all cases shown, two shock waves are observed. The first one is the TNCSW (propagating in the water), which is emitted from the location where the two necks collide. The second one is generated by an annular depression, which propagates inside the bubble. By observing the two shock waves outside and inside the bubble, it can be noticed that the wave front of the TNCSW is convex outward, while the shock wave front inside the bubble is concave inward. The propagation direction of TNCSW is opposite to the direction of bubble contraction, and it has a weak effect on the contraction of the bubble.

Fig. 15 illustrates the neck-contraction shock wave (NCSW) of a bubble adjacent to unequal-sized dual particles. Three different values of γ have been selected to present the details of the NCSW. Compared

with Fig. 10, the difference lies in the behavior of the bubble and the location of the emitted NCSW. Owing to the considerable discrepancy between the radii of the dual particles, the neck contracts to a position close to the small particle. As a result, the location of the emitted NCSW is also close to the small particle. From Fig. 15(a) to (c), with increasing γ, the position gradually approaches the small particle, and the discrepancy in volume between the two daughter bubbles also increases. In Fig. 15(c), the particle-reflected shock wave (PRSW) is formed after the NCSW impacts the small particle.

Fig. 16 illustrates the interference of the bubble-collapse shock wave (BCSW) with the jet impact particle shock wave (JIPSW) adjacent to unequal-sized dual particles for different values of γ and δ. The different sizes of the dual particles lead to the bubble splitting into two daughter bubbles of different sizes. As a result, the tiny daughter bubble quickly collapses and produces the bubble-collapse shock wave (BCSW), while the jet of the large daughter bubble impinges on the particle surface and produces the JIPSW. In Fig. 16(a) and (b), it can be observed that the BCSW and the JIPSW are going to interfere, and in Fig. 16(c), the BCSW and JIPSW have already interfered. When BCSW encounters the large daughter bubble, it will intensify the collapse of the large daughter bubble.

8. Conclusions

Numerical simulations of cavitation bubble evolution adjacent to single and dual particles have been performed based on the OpenFOAM solver with experimental validations. Specifically, the generation and propagation of shock waves have been investigated by a numerical schlieren approach. For the dual particles, the development of a bubble neck structure determines the shock wave generation mechanism. The primary conclusions of this study are given as follows:

1. At bubble inception, an inception shock wave (ISW) is emitted, which will be reflected multiple times between the bubble interface and the particle surface. As the bubble-particle distance increases, the pressure induced by the ISW or its reflected shock wave on the particle decreases. During bubble collapse, the jet initially pierces the bubble, generating the jet-pierce shock wave (JPSW). Subsequently, the jet continues to impinge on the particle, generating the jet impact particle shock wave (JIPSW) in the opposite direction of the jet.
2. For dual particles with equal sizes, a neck contraction to the symmetry axis of the bubble produces a neck contraction shock wave (NCSW) in the water and a jet-tip shock wave (JTSW) within the daughter bubble. After the generation of NCSW, its pressure significantly decreases with time and distance. As the dimensionless bubble-particle distance increases, the pressure at which NCSW is generated initially rises before subsequently decreasing. The jet-pierce shock wave (JPSW) is produced after the jet penetrating the daughter bubble.
3. For dual particles with unequal sizes, two shock waves are generated in the water and inside the bubble after the collision of the two necks, and they propagate in opposite directions. In addition, interference is observed between the bubble-collapse (BCSW) from the tiny daughter bubble and the jet impact particle shock wave (JIPSW) from the large daughter bubble jet.

CRediT authorship contribution statement

Jinsen Hu: Writing – review & editing, Writing – original draft, Resources, Methodology, Investigation, Formal analysis, Conceptualization. **Yifan Liu:** Visualization, Validation, Software, Resources. **Jingfei Duan:** Visualization, Software, Methodology. **Jiaxin Yu:** Writing – review & editing, Project administration, Formal analysis, Conceptualization. **Yuning Zhang:** Writing – review & editing, Supervision, Project administration, Methodology, Conceptualization. **Dan Gao:** Project administration, Formal analysis, Conceptualization. **Yuning Zhang:** Writing – review & editing, Supervision, Project administration, Funding acquisition.

Declaration of competing interest

The authors declare that they have no known competing financial interests or personal relationships that could have appeared to influence the work reported in this paper.

Acknowledgements

The present research was funded by the National Natural Science Foundation of China (Project No. 52076215).

References

[1] J. Sun, X. Ge, Y. Zhou, D. Liu, J. Liu, G. Li, Y. Zheng, Research on synergistic erosion by cavitation and sediment: A review, Ultrason. Sonochem. 95 (2023) 106399.
[2] G. Dan, J. Yang, L. Ge, Review of the cavitation mechanism and prevention or enhancement, Mod. Phys. Lett. B 36 (08) (2022) 2150615.
[3] A. Bußmann, F. Riahi, B. Gökce, S. Adami, S. Barcikowski, N.A. Adams, Investigation of cavitation bubble dynamics near a solid wall by high-resolution numerical simulation, Phys. Fluids 35 (1) (2023) 016115.
[4] A. Wei, L. Yu, L. Qiu, X. Zhang, Cavitation in cryogenic fluids: A critical research review, Phys. Fluids 34 (10) (2022) 101303.
[5] D. Zhao, F. Deng, L. Zhang, Numerical investigation on the impact pressure induced by a cavitation bubble collapsing near a solid wall, Phys. Fluids 35 (4) (2023) 043315.
[6] J. Yin, Y. Zhang, J. Zhu, L. Lv, L. Tian, An experimental and numerical study on the dynamical behaviors of the rebound cavitation bubble near the solid wall, Int. J. Heat Mass Transf. 177 (2021) 121525.
[7] B. Boyd, S. Becker, Numerical modeling of the acoustically driven growth and collapse of a cavitation bubble near a wall, Phys. Fluids 31 (3) (2019) 032102.
[8] J. Zhang, Y. Du, J. Liu, Y. Sun, Z. Yao, Q. Zhong, Experimental and numerical investigations of the collapse of a laser-induced cavitation bubble near a solid wall, J. Hydrodyn. 34 (2) (2022) 189–199.
[9] J. Yin, Y. Zhang, J. Zhu, L. LÜ, S.L. Li, Numerical investigation of the interactions between a laser-generated bubble and a particle near a solid wall, J. Hydrodyn. 33 (2) (2021) 311–322.
[10] P.P. Gohil, R.P. Saini, Coalesced effect of cavitation and silt erosion in hydro turbines—A review, Renew. Sustain. Energy Rev. 33 (2014) 280–289.
[11] A. Vogel, S. Busch, U. Parlitz, Shock wave emission and cavitation bubble generation by picosecond and nanosecond optical breakdown in water, J. Acoust. Soc. Am. 100 (1) (1996) 148–165.
[12] G. Lai, S. Geng, H. Zheng, Z. Yao, Q. Zhong, F. Wang, Early dynamics of a laser-induced underwater shock wave, J. Fluids Eng. 144 (1) (2022) 011501.
[13] S. Geng, Z. Yao, Q. Zhong, Y. Du, R. Xiao, F. Wang, Propagation of shock wave at the cavitation bubble expansion stage induced by a nanosecond laser pulse, J. Fluids Eng. 143 (5) (2021) 051209.
[14] J. Noack, A. Vogel, Single-shot spatially resolved characterization of laser-induced shock waves in water, Appl. Opt. 37 (19) (1998) 4092–4099.
[15] X.X. Liang, N. Linz, S. Freidank, G. Paltauf, A. Vogel, Comprehensive analysis of spherical bubble oscillations and shock wave emission in laser-induced cavitation, J. Fluid Mech. 940 (2022) A5.
[16] J. Holzfuss, M. Rüggeberg, A. Billo, Shock wave emissions of a sonoluminescing bubble, Phys. Rev. Lett. 81 (24) (1998) 5434.
[17] R. Pecha, B. Gompf, Microimplosions: Cavitation collapse and shock wave emission on a nanosecond time scale, Phys. Rev. Lett. 84 (6) (2000) 1328.
[18] M.S. Plesset, The dynamics of cavitation bubbles, J. Appl. Mech. 16 (3) (1949) 277–282.
[19] J.B. Keller, M. Miksis, Bubble oscillations of large amplitude, J. Acoust. Soc. Am. 68 (2) (1980) 628–633.
[20] A.M. Zhang, S.M. Li, P. Cui, S. Li, Y.L. L, A unified theory for bubble dynamics featured, Phys. Fluids, 35 (2023) 033323.
[21] J. Chen, B. Han, B. Li, Z. Shen, J. Lu, X. Ni, The collapse of a bubble against infinite and finite rigid boundaries for underwater laser propulsion, J. Appl. Phys. 109 (8) (2011) 083101.
[22] O. Lindau, L. Werner, Cinematographic observation of the collapse and rebound of a laser-produced cavitation bubble near a wall, J. Fluid Mech. 479 (2003) 327–348.
[23] F. Reuter, C.D. Ohl, Supersonic needle-jet generation with single cavitation bubbles, Appl. Phys. Lett. 118 (13) (2021) 134103.
[24] J. Yu, X. Wang, J. Hu, J. Shen, X. Zhang, X. Zheng, Y. Zhang, Z. Yao, Laser-induced cavitation bubble near boundaries, J. Hydrodyn. 35 (2023) 858–875.
[25] M. Zhang, Q. Chang, X. Ma, G. Wang, B. Huang, Physical investigation of the counterjet dynamics during the bubble rebound, Ultrason. Sonochem. 58 (2019) 104706.

[26] L. Tian, Y.X. Zhang, J.Y. Yin, L. Lv, J.Y. Zhang, J.J. Zhu, Study on the liquid jet and shock wave produced by a near-wall cavitation bubble containing a small amount of non-condensable gas, Int. Commun. Heat Mass Transfer 145 (2023) 106815.
[27] X. Yang, C. Liu, D. Wan, C. Hu, Numerical study of the shock wave and pressure induced by single bubble collapse near planar solid wall, Phys. Fluids 33 (7) (2021) 073311.
[28] T. Požar, V. Agrež, Laser-induced cavitation bubbles and shock waves in water near a concave surface, Ultrason. Sonochem. 73 (2021) 105456.
[29] Y. Fan, A. Bußmann, F. Reuter, H. Bao, S. Adami, Amplification of supersonic micro-jets by resonant inertial cavitation-bubble pair, Phys. Rev. Lett. 132 (2024) 104004.
[30] X. Yang, C. Liu, J. Li, Y. Yang, M. Zhao, C. Hu, Numerical study of liquid jet and shock wave induced by two-bubble collapse in open field, Int. J. Multiph. Flow 168 (2023) 104584.
[31] X. Yang, C. Liu, J. Li, M. Zhao, C. Hu, Implosion of a bubble pair near a solid surface, Phys. Rev. Fluids 8 (2023) 023602.
[32] J. Luo, W. Xu, B. Khoo, Stratification effect of air bubble on the shock wave from the collapse of cavitation bubble, J. Fluid Mech. 919 (2021) A16.
[33] P. Cui, A. Zhang, S. Wang, Y. Liu, Experimental study on interaction, shock wave emission and ice breaking of two collapsing bubbles, J. Fluid Mech. 897 (2020) A25.
[34] O. Supponen, D. Obreschkow, P. Kobel, M. Tinguely, N. Dorsaz, M. Farhat, Shock waves from nonspherical cavitation bubbles, Phys. Rev. Fluids 2 (9) (2017) 093601.
[35] Z. Tan, M. Zhang, G. Huang, B. Huang, collapsing behavior of a spark-induced cavitation bubble near the air bubble attached to the tube nozzle, Ocean Eng. 253 (2022) 111183.
[36] Y. Dai, H. Zhang, T. Chen, Influence of bubble-particle distance on the dynamic behaviors of a cavitation bubble near a particle, J. Hydrodyn. 35 (5) (2023) 913–922.
[37] S. Li, R. Han, A.M. Zhang, Nonlinear interaction between a gas bubble and a suspended sphere, J. Fluids Struct. 65 (2016) 333–354.
[38] B.H.T. Goh, S.W. Gong, S.W. Ohl, B.C. Khoo, Spark-generated bubble near an elastic sphere, Int. J. Multiph. Flow 90 (2017) 156–166.
[39] S. Poulain, G. Guenoun, S. Gart, W. Crowe, S. Jung, Particle motion induced by bubble cavitation, Phys. Rev. Lett. 114 (21) (2015) 214501.
[40] L.A. Teran, S. Laín, S.A. Rodríguez, Prediction of the particle's impact velocity due to the bubble–particle interaction causing synergic wear, Tribol. Int. 180 (2023) 108261.
[41] D. Chen, M. Qiu, L. Zhe, Q. Liu, G. Guang, Z. Zhu, Experimental study on the interaction of a cavitation bubble flanked by two particles, Acta Mech. 232 (2021) 4801–4810.
[42] J. Zevnik, M. Dular, Cavitation bubble interaction with a rigid spherical particle on a microscale, Ultrason. Sonochem. 69 (2020) 105252.
[43] L. Zou, J. Luo, W. Xu, Y. Zhai, J. Li, T. Qu, G. Fu, Experimental study on influence of particle shape on shockwave from collapse of cavitation bubble, Ultrason. Sonochem. 101 (2023) 106693.
[44] J. Hu, X. Lu, Y. Liu, J. Duan, Y. Liu, J. Yu, X. Zheng, Y. Zhang, Numerical and experimental investigations on the jet and shock wave dynamics during the cavitation bubble collapsing near spherical particles based on OpenFOAM, Ultrason. Sonochem. 99 (2023) 106576.
[45] J. Hu, Y. Liu, Y. Liu, J. Duan, X. Lu, X. Zheng, J. Yu, Y. Zhang, Y. Zhang, Numerical investigation of cavitation bubble jet dynamics near a spherical particle, Symmetry 15 (9) (2023) 1655.
[46] C.J. Greenshields, OpenFOAM v10 User Guide, The OpenFOAM Foundation, London, UK, 2022.
[47] H.G. Weller, G. Tabor, H. Jasak, C. Fureby, A tensorial approach to computational continuum mechanics using object-oriented techniques, Comput. Phys. 12 (1998) 620–631.
[48] G. Xia, W. You, S. Manickam, J.Y. Yoon, X. Xuan, X. Sun, Numerical simulation of cavitation-vortex interaction mechanism in an advanced rotational hydrodynamic cavitation reactor, Ultrason. Sonochem. 105 (2024) 106849.
[49] X. Sun, G. Xia, W. You, X. Jia, S. Manickam, Y. Tao, S. Zhao, J.Y. Yoon, X. Xuan, Effect of the arrangement of cavitation generation unit on the performance of an advanced rotational hydrodynamic cavitation reactor, Ultrason. Sonochem. 99 (2023) 106544.
[50] H.T. Chen, R. Collins, Shock wave propagation past an ocean surface, J. Comput. Phys. 7 (1) (1971) 89–101.
[51] Q. Zeng, S.R. Gonzalez-Avila, C.D. Ohl, Splitting and jetting of cavitation bubbles in thin gaps, J. Fluid Mech. 896 (2020) A28.
[52] X. Zheng, X. Wang, X. Lu, J. Yuan, Y. Zhang, Y. Zhang, Experimental research on the collapse dynamics of the cavitation bubble near two spherical particles, J. Mech. Sci. Technol. 37 (5) (2023) 2451–2460.